Journal of Materials Chemistry C

PAPER

View Article Online
View Journal | View Issue

Cite this: J. Mater. Chem. C, 2017, 5, 9296

Highly efficient field emission from ZnO nanorods and nanographene hybrids on a macroporous electric conductive network

Chi Zhang,[a] Dajun Wu,[a] Xin Tong,[a] Yiping Zhu,*[ab] Shaohui Xu,[a] Dayuan Xiong,[ab] Pingsheng Guo,[c] Yishan Wu,[c] Ruijuan Qi,[a] Rong Huang,[a] Lianwei Wang,*[ab] Shaoqiang Chen[a] and Paul K. Chu[d]

Received 24th June 2017,
Accepted 4th August 2017

DOI: 10.1039/c7tc02821k

rsc.li/materials-c

A hybrid structure comprising zinc oxide (ZnO) nanorods and nanographene on a patterned substrate enhances the field emission properties by reducing the work function, avoiding electrostatic screening, and providing more emitters. A theoretical energy-band model is fabricated to analyze the field emission process of the ZnO nanorods and nanographene hybrids. And the structure is modeled with equipotential lines and simulated by Ansys to present the advantages of the three-dimensional (3D) patterned substrate. After theoretical modeling and simulation, a simple, low-cost, and environmentally friendly method that is suitable for industrial production is developed to fabricate ZnO nanorods and nanographene hybrids on a 3D macroporous electric conductive network (MECN). The nanographene is coated on the MECN by hydrothermal carbonization to circumvent the substrate limitation and ZnO nanorods are prepared on the nanographene/MECN substrate hydrothermally. The ZnO nanorods, ~600 nm long with a diameter of about 70 nm, in combination with nanographene show sharp edges and an ordered lattice pattern and, therefore, electrons flow from the nanographene to the ZnO nanorods and are emitted more easily. The ZnO nanorods/nanographene/MECN has highly efficient field emission properties such as a low turn-on voltage E_{on} of 0.5 V μm^{-1} at a current density of 10 $\mu A\ cm^{-2}$, and a large field enhancement factor β of 25550, as well as excellent sustainability and consequently great potential in displays, lighting, and sensors.

1. Introduction

Electron field emission is a quantum-tunneling phenomenon in which electrons are emitted from a cathode to an anode in the presence of an applied electric field. High-quality field emitters are preferred for vacuum microwave amplifiers,[1] field emission scanning electron microscopes,[2] and flat panel displays.[3] A small work function and dense sharp edges are vital for efficient field emission[4] and nanostructured materials such as graphene,[5] carbon nanotubes,[6] zinc oxide (ZnO),[7] and tin dioxide (SnO_2)[8] and their combinations have been reported to be field-emission materials. As a wide band gap metal-oxide semiconductor material (3.37 eV), ZnO has attracted much attention due to its favorable electrical properties. For instance, ZnO has a large exciton binding energy (60 MeV) at room temperature, low electron affinity, and high thermal stability. Since the properties of ZnO are affected by its morphology and the large shape anisotropy of ZnO nanorods facilitates field emission, hydrothermal synthesis,[9] chemical deposition,[10] electrophoresis,[11] chemical vapor deposition (CVD)[12] and physical vapor deposition (PVD)[13] have been used to produce ZnO nanorods[14,15] or nanosheets.[16]

Graphene with a 2D (two-dimensional) structure has been applied to energy storage, solar cells, sensors, catalysts, and electron field emitters.[17–19] Composed of mono-layer sp^2 carbon atoms in a honeycomb crystal lattice, graphene has superior electrical conductivity, mechanical flexibility, and good chemical/thermal stability. In recent studies, ZnO/graphene hybrid nanostructures have shown promise in field emission. Zheng *et al.*[20] prepared a composite of graphene sheets and ZnO nanowires by vapor phase deposition and

[a] Key Laboratory of Polar Materials and Devices, Ministry of Education, and Department of Electronic Engineering, East China Normal University, 500 Dongchuan Road, Shanghai 200241, China. E-mail: lwwang@ee.ecnu.edu.cn, ypzhu@ee.ecnu.edu.cn; Fax: +86-21-54345119; Tel: +86-21-54345160
[b] Shanghai Key Laboratory of Multidimensional Information Processing, East China Normal University, Shanghai 200241, China
[c] Engineering Research Center for Nanophotonics & Advanced Instrument, Ministry of Education, and Department of Physics, East China Normal University, 3663 North Zhongshan Road, Shanghai 200062, China
[d] Department of Physics and Material Science, City University of Hong Kong, Tat Chee Avenue, Kowloon, Hong Kong, China

plasma-enhanced chemical vapor deposition (PECVD) and the ZnO–graphene sheets (ZnO–GSs) showed a turn-on field of 1.3 V μm^{-1} at 1 $\mu A\ cm^{-2}$. Zhang *et al.*[14] produced uniform monolayer graphene sheets on patterned ZnO nanorod arrays by RF magnetron sputtering, hydrothermal growth, and CVD and the products had a turn-on field of 6.4 V μm^{-1} at a current density of 10 $\mu A\ cm^{-2}$. Zou *et al.*[15] utilized a simple hydrothermal method to produce sandwich-like heterostructures of ZnO/graphene/ZnO (ZnO/G/ZnO) with a turn-on field of 2.1 V μm^{-1} at a current density of 10 $\mu A\ cm^{-2}$. Graphene sheets and powders have mostly been produced by CVD and Hummer's methods. However, CVD has higher operating costs and lower efficiency than Hummer's method, which is unfortunately not environmentally friendly. Moreover, it is customary to use planar substrates to deposit graphene in both CVD and Hummer's method but planar substrates provide fewer edges and suffer from electrostatic shielding which degrades the field emission efficiency. To overcome this hurdle, Yang *et al.*[21] reported a super elastic and ultralight electron source based on 3D graphene aerogel (rGA) to optimize the field emission performance with low values of turn-on field of 1.67 V μm^{-1}. Yan *et al.*[22] prepared ordered carbon nanotube (CNT)–ZnO heterojunction arrays on pyramid-like micropatterns to show a turn-on field of 5.3 V μm^{-1}. Shao's[23] group prepared Cl-doped ZnO nanowires on 3D graphene foam and the materials showed a turn-on field of 1.6 V μm^{-1} and good stability. Yuvaraj *et al.*[24] studied the field emission properties of ZnO nanostructured films prepared by reactive evaporation and the field was 1.17 V μm^{-1} at a current density of 10 $\mu A\ cm^{-2}$ together with a large field enhancement factor of 23 213. Banerjee *et al.*[25] coated ZnO nanowires on 3D carbon cloth presenting good field emission characteristics with a field of 0.7 V μm^{-1} at a current density of 1 mA cm^{-2} and high enhancement factor of 41 100. The above-mentioned results suggest that hybrids of ZnO and carbon materials such as graphene nanostructures prepared on a patterned 3D substrate may have excellent field emission characteristics.

Herein, in order to avoid the electrostatic shielding effect and enhance the field emission performance, a patterned 3D substrate consisting of porous array nickel-coated silicon microchannel plates (Si-MCPs), which constitute a macroporous electric conductive network (MECN), was proposed to fabricate a 3D structure field emission device. The ordered lattice of the MECN provides dense sharp edges and avoids electrostatic shielding effectively. Additionally, nanographene can be coated on it uniformly.[26,27] Then a ZnO nanorod/nanographene hybrid is prepared on the MECN to achieve outstanding field emission properties. This hybrid structure is systematically investigated by theoretical modeling, simulation, and actual testing.

2. Experimental section

2.1 Materials and characterization

All used chemicals are purchased from Sinopharm Chemical Reagent Co. Ltd and used without further purification. All aqueous solutions are prepared using 18 MΩ deionized water. X-ray diffraction (XRD) was performed using a Rigaku RINT2000 and the ZnO nanorods/nanographene/MECN was characterized using a micro-Raman system (DXR Microscope, Thermo Fish, USA) equipped with a charged coupled detector and a 515 nm Ar laser. The transmittance spectra of ZnO nanorods/nanographene/MECN, ZnO nanorods/MECN, and nanographene/MECN were obtained by UV-Vis spectroscopy (UV-VIS-NIR; Shimadzu, UV-3600, Japan). The elements of ZnO nanorods/nanographene/MECN were determined by X-ray photoelectron spectrometry (XPS) using the Mg Kα line and a PHOIBOS100MCD energy analyzer under an ultra-high vacuum (10^{-10} mbar). The morphology was examined using a field-emission scanning electron microscope (FE-SEM; JEOL, JSM-7001F, Japan) equipped with an energy-dispersive X-ray spectrometer and the microstructure was investigated by high-resolution transmission electron microscopy (HRTEM; JEOL, JEM-2001F, Japan). The work function of nanographene and the work function of the ZnO nanorod/nanographene hybrids were characterized by ultraviolet photoelectron spectroscopy (UPS; Gamma data Scienta, Scientases 200, Sweden).

2.2 Preparation of nanographene/MECN

Si-MCPs were prepared by a microelectromechanical system (MEMS) process. After cleaning, oxidation, photolithography, wet etching and photo-assisted electrochemical etching, the Si-MCPs with a square array of channels 250 μm deep and 5 × 5 μm pores were obtained. The walls between pores were 1 μm thick. More details about the process can be found in ref. 28.

The nickel films were produced by electroless deposition.[29] Ammonium chloride (NH_4Cl, 10 g), sodium hypophosphite hydrate ($NaH_2PO_2{\cdot}H_2O$, 2 g), and nickel chloride hexahydrate ($NiCl_2{\cdot}6H_2O$, 6 g) were dissolved in an aqueous solution (200 ml) and NH_4OH was added to adjust the pH to 9–11. The 1 × 1 cm^2 Si-MCP was immersed in the solution ($HF : C_2H_5OH : H_2O = 100 : 125 : 10$, V/V) for 10 minutes to remove the native oxide and then put in the electroless deposition solution at 90 °C for 20 minutes. Afterwards, the samples were dried at 80 °C overnight in a vacuum oven to produce the MECN.

A sodium sulfate (Na_2SO_4, 1 ml, 1 M) solution was added dropwise to triethylene glycol (TEG, 20 ml) to prepare the hydrothermal carbonization solution.[30] The solution was stirred magnetically for 30 minutes at room temperature and the as-prepared MECN was added and sonicated for 1 minute to purge the air from the channels. Afterwards the sample and the solution were transferred to a 25 ml Teflon-sealed stainless steel autoclave and heated to 260 °C for 6 hours converting Ni into Ni_3C. The samples were washed with deionized water and absolute ethyl alcohol three times and dried at 80 °C under vacuum overnight. Finally, the samples were annealed at 650 °C for 30 minutes under flowing Ar gas (500 sccm) dividing Ni_3C into nanographene and a Ni film.

2.3 Preparation of ZnO nanorods/nanographene/MECN and ZnO nanorods/MECN

Zinc acetate [$Zn(CH_3COO)_2{\cdot}2H_2O$, 20 mM] was dissolved in ethanol to form the template solution in which the MECN

and nanographene/MECN were immersed under vacuum for several minutes. The samples were dried at 80 °C under ambient conditions, annealed at 300 °C for 1 hour under Ar at a heating rate of 10 °C min^{-1}, and cooled naturally.

Zinc nitrate hexahydrate ($Zn(NO_3)_2 \cdot 6H_2O$, 25 mM) and hexamethylenetetramine (HMT, 25 mM) were dissolved in water to form the hydrothermal solution. The samples with templates and hydrothermal solution were transferred to a 25 ml Teflon-sealed stainless steel autoclave and heated to 90 °C for 4 hours. The samples were then rinsed with deionized water and absolute ethyl alcohol three times and dried at 80 °C under vacuum overnight.[9]

2.4 Field emission measurement

The field emission characteristics were determined based on a diode structure in a vacuum chamber at 1×10^{-4} Pa. A phosphor-coated indium tin oxide (ITO) glass piece was the anode and the sample adhered to another piece of ITO glass with conductive silver was the cathode. The distance (d) between the sample and anode was 100 μm and the sample area (A) was 1 cm^2. The electric field (E) was calculated by dividing the applied voltage (V) by the distance ($E = V/d$). The current density (J) was estimated by dividing the current (I) by the area ($J = I/A$). The samples were pre-emitted for 2 or 3 cycles between 100 V and 600 V before the actual measurement. To analyze the field emission characteristics, the turn-on field (E_{on}) was defined as the electric field required for a current density of 10 μA cm^{-2}.

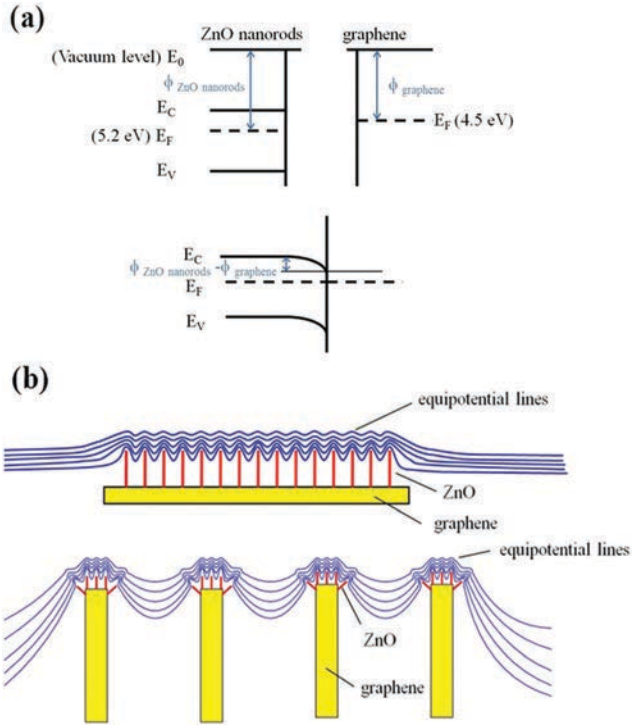

Fig. 1 (a) Schematic theoretical energy band diagram of ZnO nanorods and graphene (top panel) and ZnO nanorods/nanographene/MECN (bottom panel). (b) Schematic plot of the equipotential lines of the typical ZnO nanorods/graphene emitter (top panel) and ZnO nanorods/nanographene/MECN (bottom panel).

3. Results and discussion

In the ZnO nanorods and nanographene hybrids structure, there are two schemes: electrons tunneling from the nanographene to the ZnO nanorods are emitted from the ZnO nanorods and on the other hand, electrons tunneling from the ZnO nanorods to the nanographene are emitted from the nanographene. Fig. 1a shows the theoretical energy-band diagram of the ZnO nanorods/nanographene structure with the ZnO nanorods as an n-type semiconductor with a work function of 5.2 eV ($\phi_{ZnO\ nanorods}$ = 5.2 eV)[31] and nanographene being metallic with a work function of 4.5 eV ($\phi_{nanographene}$ = 4.5 eV).[32] When they are put together, a semiconductor–metal junction is formed. The energy band of the ZnO nanorods bends downwards because the work function of the ZnO nanorods is larger than that of the nanographene ($\phi_{ZnO\ nanorods} > \phi_{nanographene}$). Electrons flow from the nanographene to the ZnO nanorods forming a negative space charge region and the internal electric field direction is from the vacuum to the substrate. Hence, in this work, the first scheme in which electrons tunnel from the nanographene to the ZnO nanorods is adopted. In this case, the direction of the applied electron field is the same as that of the built-in electric field which contributes to the field emission. The contact barrier becomes the work function difference between the ZnO nanorods and nanographene ($\phi_{ZnO\ nanorods} - \phi_{nanographene}$). When the applied voltage is increased, the electric field intensifies and electrons tunnel through the barrier more readily. Schematic plots of the equipotential lines of the electric field of the ZnO nanorods are presented in Fig. 1b. Here, the substrate is planar with standing ZnO nanorods because of the limitation in graphene preparation. Although this structure can provide a lot of emission spots, it causes electrostatic screening because the ZnO nanorods are of similar altitude and arranged densely. This acts as a shield to screen the applied field which consequently reduces the voltage applied to the nanorods. To avoid electrostatic screening, a patterned 3D structure array of the MECN is preferred to increase the distance between the ZnO nanorods and amplify the fluctuations of the surface field as shown in the bottom figure. Owing to the fluctuations caused by the ordered array of the MECN, the shield is broken and the electrostatic screening is avoided. Also, there are adequate ZnO nanorods to facilitate electron emission.

To illustrate this model and explore the possibility and feasibility of this structure, the distribution of the electric potential and electric field of the ZnO nanorods/nanographene structure on the MECN substrate (ZnO nanorods/nanographene/MECN) are simulated by Ansys (V. 15.0) as shown in Fig. 2a and c. Fig. 2b and d are magnifications of Fig. 2a and c, respectively. The potential distributions are estimated by finite difference and the electric field gradients are calculated using the fourth-order Runge–Kutta formalism. In the simulation, the vacuum is set as the absolute vacuum. The distance between the anode and cathode is 3 μm and the applied voltage is 3 V maintaining an actual electric field of 1 V μm^{-1}. The big

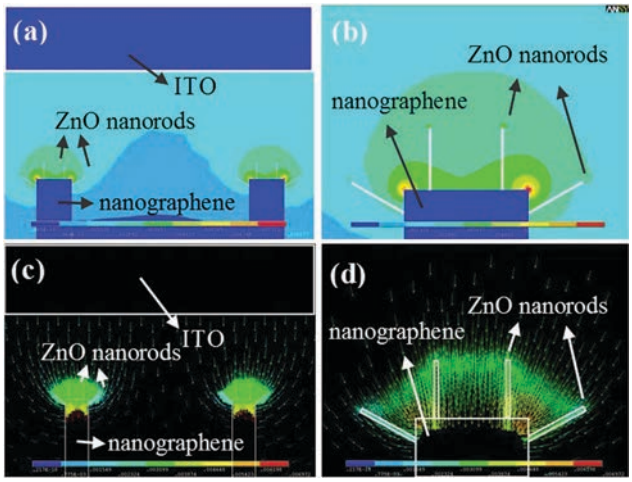

Fig. 2 (a) Simulated potential distribution (color bar, *V*) at the ZnO nanorods/nanographene/MECN. (b) Magnification of (a). (c) Simulated electric field (color bar, *E*) at the ZnO nanorods/nanographene/MECN. (d) Magnification of (c).

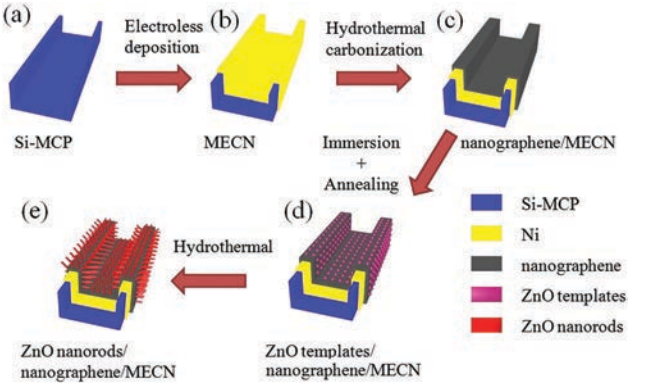

Fig. 3 Schematic illustrating the synthesis procedure of ZnO nanorods/nanographene/MECN: (a) Si-MCP; (b) MECN; (c) nanographene/MECN; (d) ZnO templates/nanographene/MECN; (e) ZnO nanorods/nanographene/MECN.

rectangle in the top is set as ITO glass. The two rectangles on the bottom represent Si-MCP walls coated by nanographene. The tiny rectangles on the Si-MCP walls are set as ZnO nanorods. According to Fig. 2a and c, the top of each ZnO nanorod shows field emission performance separately. At the same time, they exhibit group and mutual effects. From Fig. 2a, the apparent undulating changes of electric potential can be seen between the walls due to the lattice pattern of the MECN. The undulations reduce electrostatic shielding contributing to field emission behavior that agrees with the theoretical model. As shown in Fig. 2b and d, the electrons are emitted from the top of the ZnO nanorods and more intense field emission can be attained with a denser distribution of ZnO nanorods. The sharp edges of the substrate also improve the field emission properties that can be seen in the corners of the walls. The patterned MECN coated with nanographene has sharp edges and surface defects to reduce the work function. Fig. 2d shows the enlarged electric field at the contact between the ZnO nanorods and nanographene due to the higher mobility of the electrons of the contact. The simulation results verify the validity of the model suggested earlier.

Following the support of theoretical analysis and simulation, the ZnO nanorods/nanographene/MECN structure is prepared experimentally as illustrated in Fig. 3. The p-type silicon is processed by one-step photo-assisted electrochemical etching[28] and the Ni film is coated on the surface and the sidewalls of the Si-MCP by electroless deposition to form the MECN. Nanographene is then deposited on the MECN by hydrothermal carbonization and the ZnO template is prepared to form the ZnO nanorods. Vacuum immersion and annealing are employed to deposit the ZnO template on nanographene/MECN and the ZnO nanorods are produced by a one-step hydrothermal process on the ZnO templates finally.

The XRD patterns in Fig. 4a are assigned according to the PDF card. Ni has three sharp peaks: (111) at 44.6°, (200) at 51.9°, and (220) at 76.6° (#70-0989). The strongest peak at 69.1° is indexed to the Si (#77-2109). The trace graphite (002) peak of ZnO nanorods/nanographene/MECN and nanographene/MECN at 26.1° is shown as the blue and green lines. The remaining peaks are (100) at 31.7°, (002) at 34.4°, and (101) at 36.2° attributable to ZnO (#89-1397). The strong (002) diffraction peak indicates highly oriented *c*-axis rod-like crystal growth. There are rarely obvious disturbances, which indicates no impurity compounds. The Raman image of ZnO nanorods/nanographene/MECN obtained with a 515 nm laser (Fig. 4b) reveals two main peaks for Zn[33] and three main peaks for nanographene. The strong peaks at 101 cm^{-1} and 437 cm^{-1} correspond to the E_2(low) and E_2(high) modes of ZnO, respectively. The E_2(low) peak results from the vibration of the Zn sub-lattice and the E_2(high) peak is related to the oxygen atoms. The strong E_2(high) mode indicates a sharp morphology of the wurtzite ZnO nanorod crystals. From the inset magnification, the D-band, G-band, and symmetric 2D-band are at 1350 cm^{-1}, 1590 cm^{-1} and 2780 cm^{-1}, respectively. The D-band originates from backscattering of phonons by disorder and the G-band is associated with sp^2 carbon. The 2D-band is assigned to the number of layers of graphene. The strong D peak indicates the presence of defects in nanographene to decrease the work function to facilitate field emission. The 2D-band is weak and so the I_{2D}/I_G ratio is small. Since the integrated intensity ratio of the 2D to G band indicates the number of graphene layers, the nanographene coated on the MECN has a multi-layered nanographene structure. The results show that the nanographene in ZnO nanorods/nanographene/MECN has many defects where the gaps and sharp edges serve as active emission sites for field emission. The optical transparency of ZnO nanorods/nanographene/MECN, ZnO nanorods/MECN, and nanographene/MECN is measured by UV-Vis spectroscopy as shown in Fig. 4c. Although nanographene/MECN is mostly composed of silicon with poor optical transparency, the porous structure offers a certain optical transparency. Owing to the intrinsic transparency of ZnO with a wide band gap, the transparency of the ZnO nanorods/MECN is increased. And the vertical alignment and uniform distribution

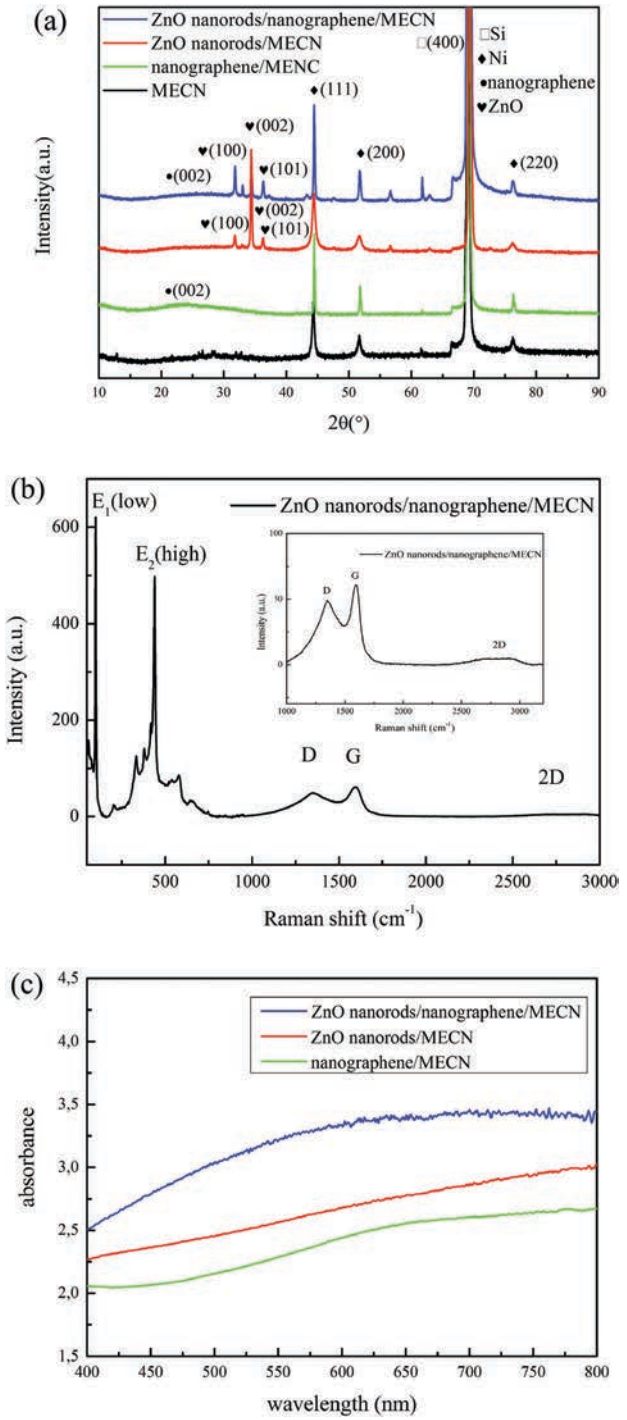

Fig. 4 (a) XRD patterns of ZnO nanorods/nanographene/MECN as well as ZnO nanorods/MECN, nanographene/MECN, and MECN. (b) Raman spectra of ZnO nanorods/nanographene/MECN. (c) UV-Vis spectra of ZnO nanorods/nanographene/MECN as well as ZnO nanorods/MECN, and nanographene/MECN.

of well crystallized sharp ZnO nanorods support a high optical transparency of the ZnO nanorods/nanographene/MECN from the red line in Fig. 4c.[10]

Fig. 5a shows the typical XPS wide survey spectrum of ZnO nanorods/nanographene/MECN, and the inset shows the atomic percentages of C (52.75 at%), Ni (2.88 at%), Si (7.45 at%), Zn (10.76 at%), and O (27.16 at%). No extra peak corresponding to magnetic impurities is observed in this wide survey spectrum. The C, Zn, and O peaks were detected as shown in the three wide survey spectra in Fig. 5b–d. As shown in Fig. 5b, two dominant peaks at 285.1 eV and 284.3 eV correspond to sp^2-C and sp^3-C, respectively and a small peak at 288.5 eV corresponds to C–OO in the C 1s high-resolution spectrum.[34] The intensity of sp^2-C is high which represents the nanographene. From Fig. 5c, the O 1s spectrum is fitted with three Gaussian peaks centered at 530.6 eV, 531.4 eV, and 532.2 eV. These high binding energy components are attributed to the presence of loosely bound oxygen on the surface of the sample, belonging to a specific species, *e.g.*, $-CO_3$, adsorbed H_2O or adsorbed O_2.[35,36] The peak of the low binding energy at 529.1 eV is attributed to O^{2-} ions in the Zn–O bonding on the wurtzite structure of the hexagonal Zn^{2+} ion array.[37] The Zn 2p spectrum in Fig. 5d shows two peaks with binding energies of 1021.5 eV and 1044.4 eV. They are identified as Zn $2p_{3/2}$ and Zn $2p_{1/2}$, respectively. The binding energy difference between the two lines is 22.9 eV, which is lying well within the standard reference value of ZnO.[38]

The SEM patterns of the as-prepared Si-MCP are shown in Fig. 6a and b. The SEM image of the MECN with a square lattice shape is shown in Fig. 6a. The Si-MCP is composed of a square lattice array with 5 × 5 μm pores and 1 μm thick walls. The patterned substrate provides abundant edges and the right distance between the walls for field emission. According to the cross-sectional SEM image in Fig. 6b, the 3D substrate has vertical inside walls. The latticed structure is not easy to be bent or distorted, thus increasing its usable life. This indicates good mechanical properties leading to good stability in field emission.[28] The length of the MECN is about 250 μm. As shown in Fig. 6c, the nickel current collector has good uniformity and retains the original ordered morphology. The SEM pattern of nanographene/MECN is depicted in Fig. 6d. During Ni-assisted hydrothermal carbonization, nanographene is coated on the surface and walls of the MECN uniformly and continuously. This indicates that nanographene was coated well following the lattice of MECN. Therefore, this method circumvents the substrate limitation common to traditional graphene preparation methods. At the same time, the nanographene has ripples and wrinkles typical of graphene sheets due to the small thickness and thermodynamic characteristics that also provide more emission points. The Fig. 6e shows the SEM image of the ZnO nanorods/MECN and Fig. 6f is the magnified image of Fig. 6e. Since the hydrothermal process is mature as per the previous literature, different conditions for the templates were taken to prepare the ZnO nanorods. The template concentration is the key factor and annealing is essential. After optimization, the recipe above was chosen to prepare ZnO nanorods with good crystallization. According to Fig. 6e and f, ZnO nanorods with a length of 200 nm and diameter of 50 nm are produced on the MECN. The nanorods on the Ni electric collector are sparse with small aspect ratios. There are some large rod-like crystals on the surface. They are also ZnO but caused by defects. This can be confirmed by the XRD pattern

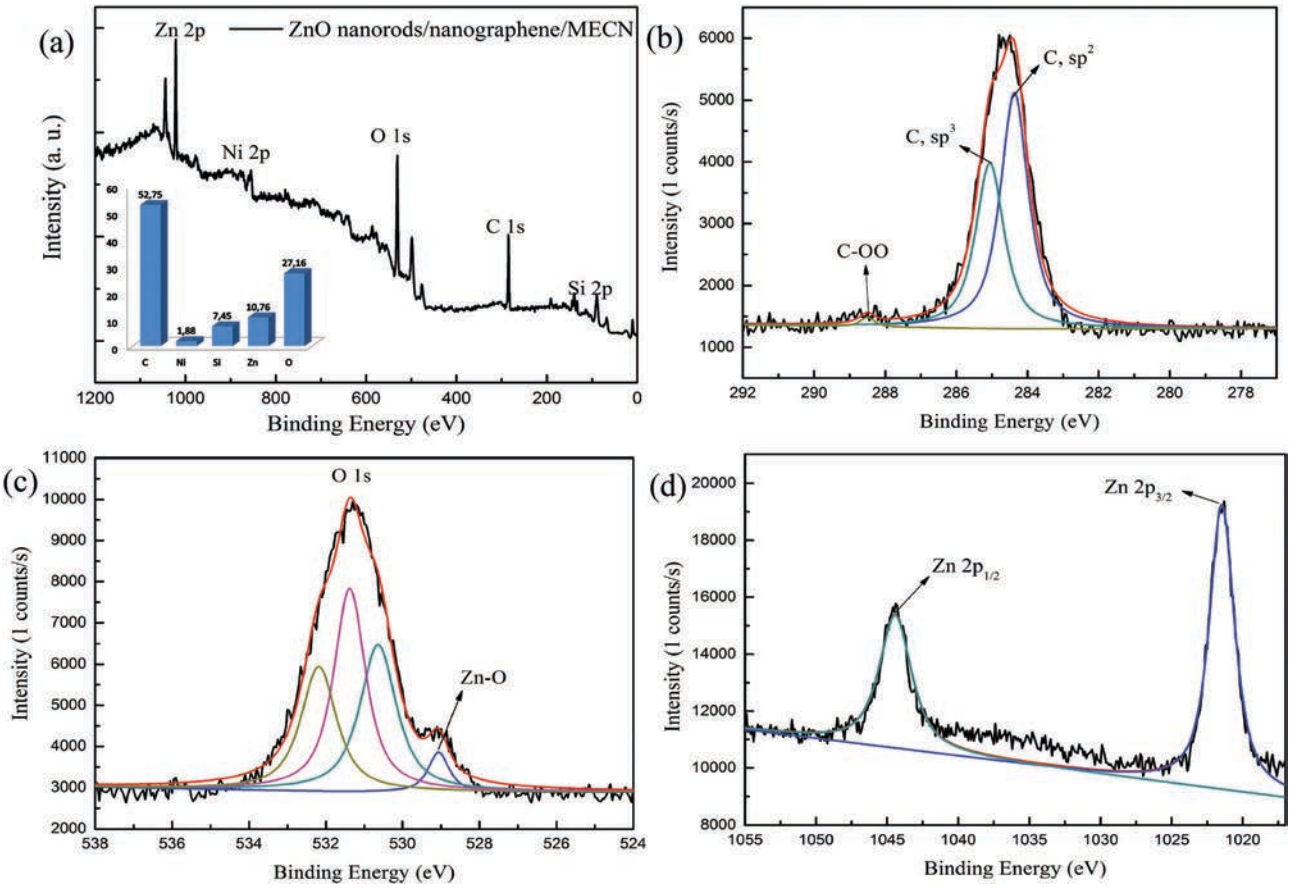

Fig. 5 XPS images: (a) the typical XPS wide survey spectrum of ZnO nanorods/nanographene/MECN. (b) High-resolution C 1s spectrum. (c) High-resolution O 1s spectrum. (d) High-resolution Zn 2p spectrum.

with no obvious impure peaks. The big-size ZnO crystals are grown based on some defects instead of templates. They are not as sharp as the nanorods so their field emission performance can be ignored. Fig. 7a–d show a series of SEM images of the ZnO nanorods/nanographene/MECN and Fig. 7b–d are magnified images of Fig. 7a. ZnO nanorods with a length of 600 nm and diameter of 70 nm are formed on the nanographene/MECN vertically and uniformly and different from deposition on the MECN without nanographene, the ZnO nanorods on nanographene/MECN have larger aspect ratios and are denser. From Fig. 7d, the cross-section of the ZnO nanorods is hexagon thus providing more edges for field emission and the morphology of the ZnO nanorods corresponds to the (002) diffraction peak in the XRD pattern.

The TEM images of the ZnO nanorods/nanographene/MECN are shown in Fig. 8. As shown in Fig. 8a, the length of the ZnO nanorods is about 600 nm and the diameter is about 70 nm consistent with the morphology revealed by SEM. The ZnO nanorods stand on the nanographene/MECN and the TEM image for the nanographene obtained from the blue area is displayed in Fig. 8b. Ni forms spherical particles around which nanographene is deposited and the Ni lattice spacing is 0.20 nm. The lattice spacing of nanographene is 0.36 nm and the thickness of the nanographene film is about 6 nm. The selected-area electron diffraction (SAED) result of the red area is shown in the inset in Fig. 8a showing the (002) peak associated with the ZnO growth direction. The high-magnification TEM image of the red area is shown in Fig. 8c and the lattice spacing is 0.26 nm corresponding to the spacing of the (002) plane of the ZnO nanorods.

The field emission properties of ZnO nanorods/nanographene/MECN are measured using a diode structure in a vacuum chamber at 1×10^{-4} Pa and at room temperature. The ZnO nanorods/MECN, nanographene/MECN, and MECN are also studied under the same experimental conditions for comparison. Fig. 9a shows the electron field emission current density (J) *versus* applied electric field (E). The turn-on voltages defined as the field required for a current density of 10 μA cm^{-2} are determined to be 0.5 V μm^{-1}, 0.7 V μm^{-1}, 2.1 V μm^{-1}, and 4.7 V μm^{-1}. The ZnO nanorods/nanographene/MECN shows an excellent high current density of 500 μA cm^{-2} at a low voltage of 1.8 V μm^{-1}, which is larger than those of ZnO nanorods/MECN of 450 μA cm^{-2} at 2.5 V μm^{-1}, nanographene/MECN of 460 μA cm^{-2} at 2.9 V μm^{-1} and MECN of 460 μA cm^{-2} at 5.2 V μm^{-1}. Comparing ZnO nanorods/nanographene/MECN with ZnO nanorods/MECN, the sample with nanographene has a smaller turn-on field and this can be explained by the morphology of the ZnO nanorods. As shown by SEM, the ZnO nanorods on

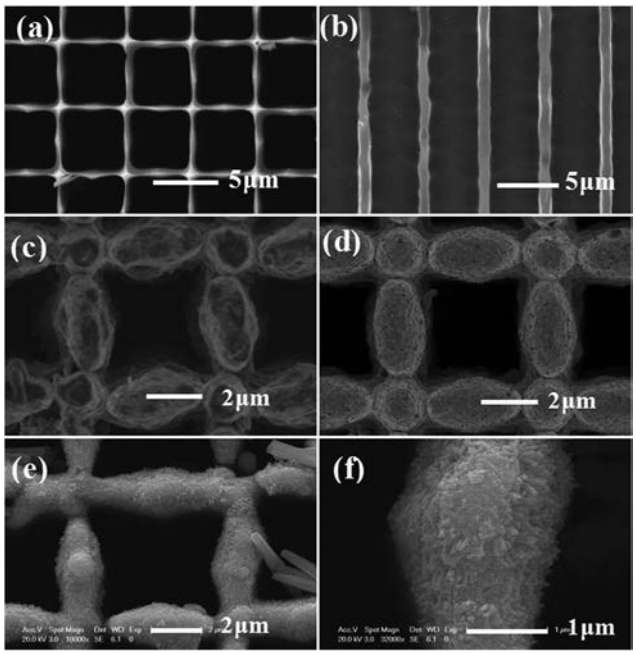

Fig. 6 SEM images: (a) Top view of Si-MCP. (b) Cross-section of Si-MCP. (c) Top view of MECN. (d) Top view of nanographene/MECN. (e) Top view of ZnO nanorods/MECN. (f) Magnifications of (e).

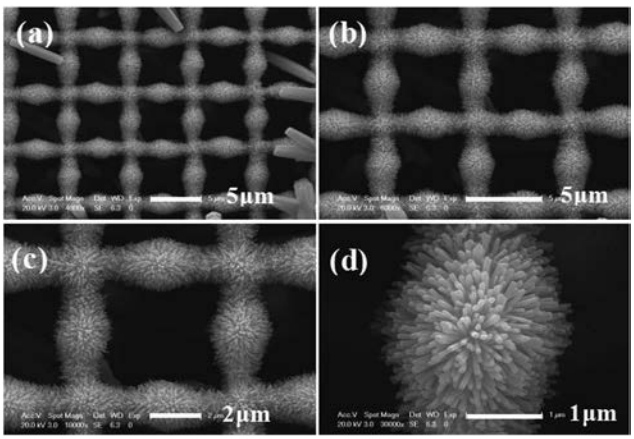

Fig. 7 (a) SEM image of the top view of ZnO nanorods/nanographene/MECN. (b–d) Magnifications of (a).

nanographene/MECN have a larger aspect ratio and denser distribution than those on MECN. The ZnO nanorods with more sharp edges are more efficient field emission spots. The ZnO nanorods prepared are more n-type due to the hydrothermal method whereas nanographene is metallic owing to its good conductivity. When they are in contact, electrons flow from nanographene to ZnO to achieve thermal equilibrium at the metal–semiconductor junction and hence, the ZnO nanorods and nanographene hybrid deliver superior performance. The ZnO nanorods/nanographene/MECN has a smaller turn-on field than nanographene/MECN.

To further analyze the field emission properties of the samples, we used the Fowler–Nordheim (F–N) theory, a common

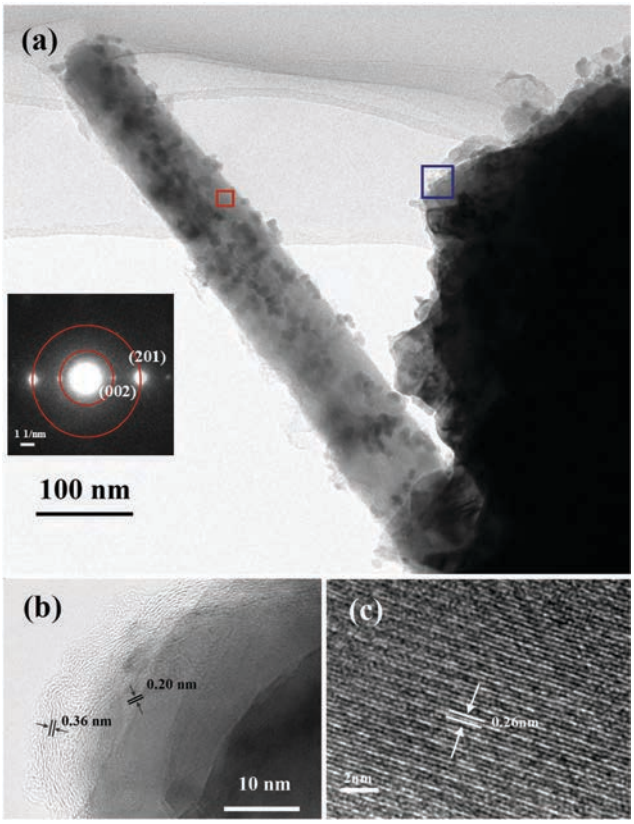

Fig. 8 (a) TEM image of ZnO nanorods/nanographene/MECN. (b) High magnification TEM image for the blue block area in (a). (c) High magnification TEM image for the red block area in (a).

model to study the field emission behavior d following the F–N equation:[39]

$$J = \frac{A\beta^2 E^2}{\phi}\exp\left(\frac{B\phi^{3/2}}{\beta E}\right) \quad (1)$$

where J is the current density, A is a constant ($A = 1.56$ μA V^{-2} eV), E is the applied field, ϕ is the work function of the ZnO nanorods (5.2 eV), graphene (4.5 eV) and Ni (4.5 eV), and B is a constant ($B = 6.83 \times 10^3$ V μm^{-1} eV$^{-3/2}$). As shown in Fig. 9b, the nearly linear slopes of the plots indicate that the current results are from the field emission. The field enhancement factor β is about 25 550, 25 309, 3244, and 200 for ZnO nanorods/nanographene/MECN, ZnO nanorods/MECN, nanographene/MECN and MECN, respectively. To confirm the repeatability and sustainability, more samples in the same conditions are fabricated and measured and the J–E curves are similar. Then they are held at a certain current density for 120 minutes. As shown in Fig. 9c, the cycling performances of ZnO nanorods/nanographene/MECN for 120 minutes are investigated at current densities of 27 μA cm^{-2}, 70 μA cm^{-2} and 355 μA cm^{-2}. The deviations of the current densities are less than 8%, 16%, and 14%, respectively. The average electric fields at these current densities are 0.6 V μm^{-1}, 0.8 V μm^{-1}, and 1.3 V μm^{-1}, which are almost consistent with the J–E curve of ZnO nanorods/nanographene/MECN shown in Fig. 9a. This proves that the structure we propose and fabricate is

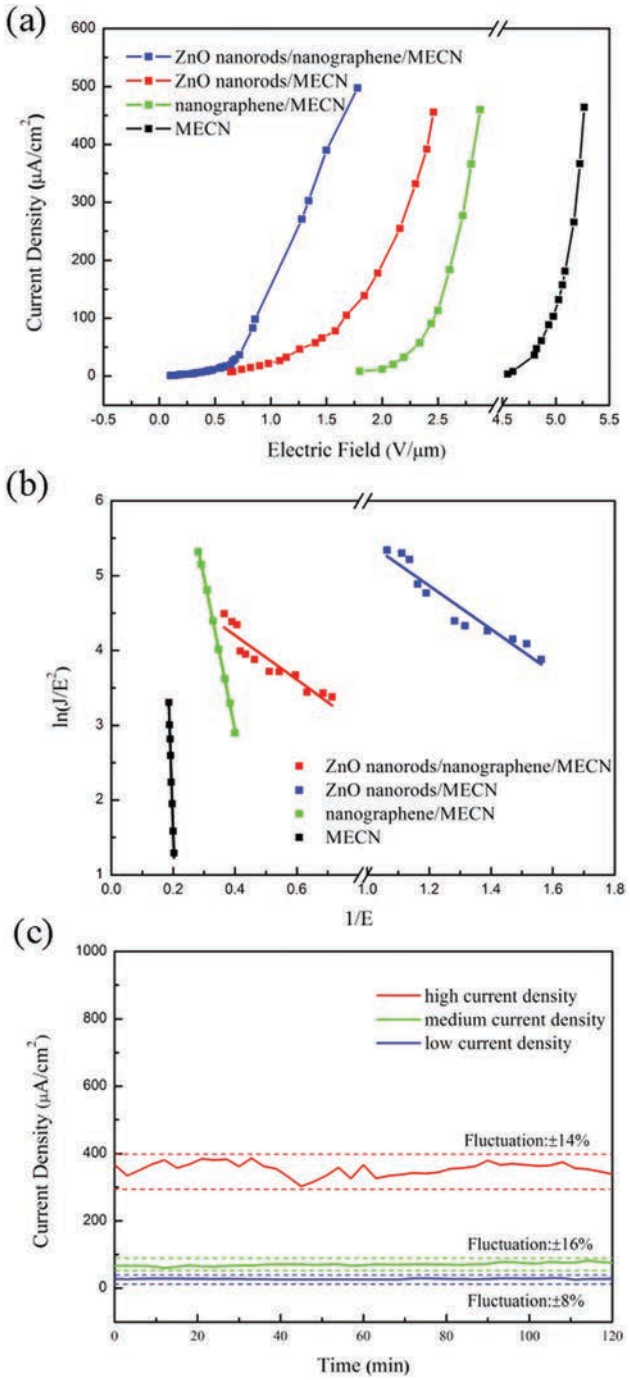

Fig. 9 (a) *J*–*E* curves of ZnO nanorods/nanographene/MECN as well as ZnO nanorods/MECN, nanographene/MECN and MECN. (b) The *F*–*N* plot of ZnO nanorods/nanographene/MECN as well as ZnO nanorods/MECN, nanographene/MECN and MECN. (c) Emission current sustainability of ZnO nanorods/nanographene/MECN for 120 min.

repeatable. Additionally, the current density of the sample is almost unchanged with good reproducibility thereby demonstrating the excellent sustainability of ZnO nanorods/nanographene/MECN. The performances of our samples are compared with the previous literature as shown in Table 1. This shows the advantages of the patterned 3D MECN as a substrate to avoid

Table 1 Field emission characteristics of some ZnO nanostructures recently reported in the literature

ZnO emitters	Turn-on field (V μm^{-1})	Enhancement factor	Ref.
Vertical ZnO nanowires on grpahene	2.0	6483	10
ZnO/G hybrid	2.72	3102	11
Cl–ZnO NWA/GF	1.6	12 844	23
ZnO nanostructure film	1.17	23 213	24
Nanorods arrays	2.98	1732	40
Propeller-like	4.36	1294	41
Nanoneedles	2.4	1464	42
ZnO nanoneedles	5.07	4166	43
Al-Doped ZnO nanowires	0.5	5583	44
ZnO nanorods /MECN	0.7	25 309	This work
ZnO nanorods/graphene/MECN	0.5	25 550	This work

electrostatic screening, the nanographene coating produced by hydrothermal carbonization, and the fabrication of ZnO nanorods as the emission materials pertaining to reduction of the barrier resistance and improvement of electron transport.

To further study the model and explain the outstanding field emission performance, the resistance of the collector was measured rather than resistivity on account of the lattice structure of the MECN. The resistance of the MECN is about 2 Ω which is suitable for current collectors in field emitters. And the resistance of nanographene/MECN diminishes to less than 1 Ω after nanographene deposition. The low resistance and good conductivity reveal that the prepared nanographene is a metal-like material. It also demonstrates that the barrier from the collector decreases because of introducing nanographene. In addition, the work functions of the field emission materials which are concerned with the theoretical model were measured by UPS. Fig. 10a shows the work function of the nanographene of 4.59 eV. It matches the theoretical model in Fig. 1a. However, the work function of ZnO nanorods coated on nanographene/MECN is not easily measured separately. The work function of the ZnO/nanographene hybrids is measured as shown in Fig. 10b. The work function of the hybrids is 4.44 eV, which is less than both the theoretical value of ZnO and the measured value of nanographene. This indicates that the contact barrier decreases due to the ZnO nanorods and nanographene heterojunction as discussed in the theoretical model. The outstanding field emission performance can be explained as follows. Firstly, MECN is a 3D patterned substrate, which provides many sharp edges, and the patterned porous structure avoids electrostatic shielding due to the uneven lattice surface. For the same reason, ZnO nanorods/MECN also has a considerable field enhancement factor. Secondly, introduction of nanographene reduces the barrier resistance between the materials and substrate and improves electron transport in the collector on account of the low resistance. Thirdly, the contact between the ZnO nanorods and nanographene being a metal–semiconductor one enables electron flow from the nanographene to the ZnO nanorods for field emission. Fourthly, the ZnO nanostructure contributes to enhanced field emission.

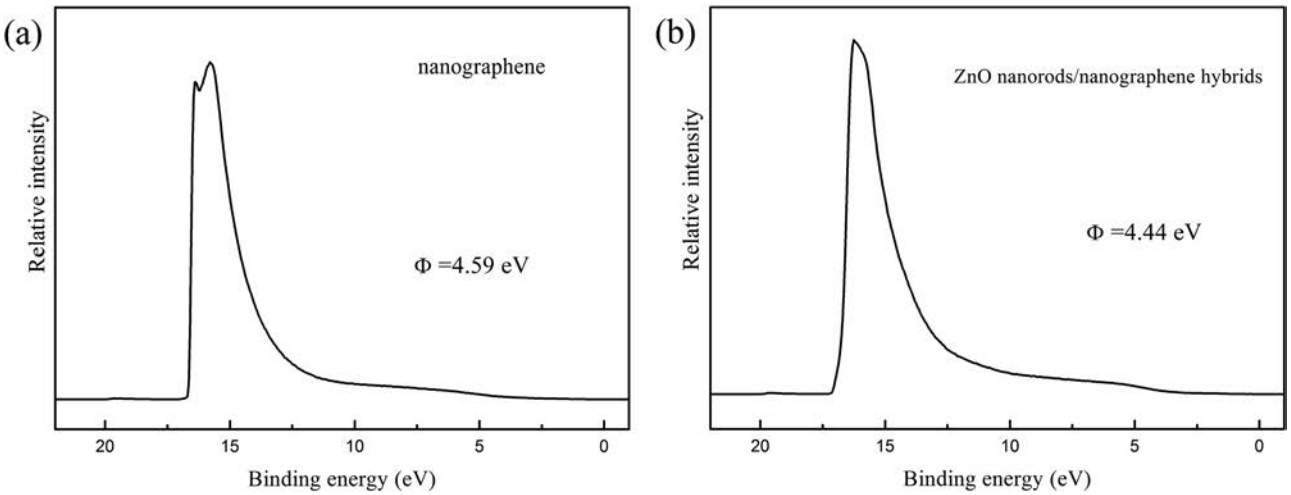

Fig. 10 (a) UPS curve of the nanographene work function. (b) UPS curve of the ZnO nanorods/nanographene hybrid work function.

4. Conclusion

A ZnO nanorods/nanographene structure is prepared on a patterned MECN substrate to improve the field emission characteristics. The properties are investigated both theoretically and experimentally. The patterned 3D conductive structure MECN substrate has an ordered lattice pattern to avoid electrostatic screening and provide more emitters. The nanographene is coated on the MECN by hydrothermal carbonization to circumvent the substrate limitation and the ZnO nanorods are prepared on the nanographene/MECN hydrothermally. The contact barrier decreases due to the formation of a ZnO nanorod/nanographene heterojunction contributing to tunneling of electrons from the nanographene to the ZnO nanorods before emission. The ZnO nanorods/nanographene/MECN possesses improved field emission properties as manifested by the low turn-on voltage (E_{on} = 0.5 V μm^{-1}) and large field enhancement factor (β = 25 550). The superiority of this outstanding field emission performance is demonstrated by comparing with present reports from other research groups. And the field emission currents of ZnO nanorods/nanographene/MECN are very stable at large, medium, and small current densities boding well for application in displays, lighting, and sensors.

Conflicts of interest

There are no conflicts to declare.

Acknowledgements

This work was jointly supported by the Shanghai Pujiang Program (No. 14PJ1403600), the National Natural Science Foundation of China (No. 61176108), the PCSIRT, Research Innovation Foundation of ECNU (No. 78210245), the Science and Technology Commission of Shanghai Municipality under research grant (No. 14DZ2260800), the Scientific Research Foundation for the Returned Overseas Chinese Scholars, State Education Ministry, the Open Research Fund of Shanghai Key Laboratory of Multidimensional Information Processing, the East China Normal University, and the City University of Hong Kong Applied Research Grant (ARG) No. 9667122. Finally, Chi Zhang gratefully acknowledges the help of Dr Xianjie Liu from Linkoping University in UPS measurements. Also, Chi Zhang would like to thank Prof. Shili Zhang and Dr. Zhibin Zhang from Uppsala University, who kindly gave her a hand.

References

1 K. T. W. Milne, E. Minoux, O. Groening, L. Gangloff, L. Hudanski, J.-P. Schnell, D. Dieumegard, F. Peauger and I. Bu, *J. Vac. Sci. Technol., B: Microelectron. Nanometer Struct.--Process., Meas., Phenom.*, 2006, **24**, 345.
2 K. A. D. J.-M. Bonard, B. F. Coll and C. Klinke, *Phys. Rev. Lett.*, 2002, **89**, 197602.
3 A. S. Q. H. Wang, J. Lauerhaas, J. Dai, E. Seelig and R. P. Chang, *Appl. Phys. Lett.*, 1998, **72**, 2912.
4 A. C. W. A. De Heer and D. Ugarte, *Science*, 1995, **270**, 1179.
5 A. K. G. K. S. Novoselov, S. Morozov, D. Jiang, Y. Zhang, S. a. Dubonos, I. Grigorieva and A. Firsov, *Science*, 2004, **306**, 666.
6 W. Y. Z. Yang, J. Lv, K. Qian, Y. Zhang, J. Liu, J. Ai, T. Guo, E. Chen and L. Hu, *J. Mater. Chem. C*, 2016, **4**, 1658.
7 J.-H. Deng, L. Cheng, F.-J. Wang, D.-J. Li and G.-A. Cheng, *Mater. Lett.*, 2015, **138**, 175–178.
8 H. He Jr, T. H. Wu, C. L. Hsin, K. M. Li, L. J. Chen, Y. L. Chueh, L. J. Chou and Z. L. Wang, *Small*, 2006, **2**, 116–120.
9 H. Ghayour, A. Nekoubin and A. A. Nourbakhsh, *Synth. React. Inorg., Met.-Org., Nano-Met. Chem.*, 2016, **46**, 975–982.
10 J. O. Hwang, D. H. Lee, J. Y. Kim, T. H. Han, B. H. Kim, M. Park, K. No and S. O. Kim, *J. Mater. Chem.*, 2011, **21**, 3432–3437.

11 J. Ding, X. Yan and Q. Xue, *Mater. Chem. Phys.*, 2012, **133**, 405–409.
12 B. Zhang, N. Binh, Y. Segawa, K. Wakatsuki and N. Usami, *Appl. Phys. Lett.*, 2003, **83**, 1635–1637.
13 T. Van Khai and T. Dai Lam, *J. Electron. Mater.*, 2016, **45**, 2601–2607.
14 L. Zhang, X. Liu, Z. Lian, X. Wang, G. Shen, D. Shen and Q. Yan, *J. Mater. Chem. C*, 2014, **2**, 3965–3971.
15 R. Zou, G. He, K. Xu, Q. Liu, Z. Zhang and J. Hu, *J. Mater. Chem. A*, 2013, **1**, 8445–8452.
16 K. Mahmood, S. B. Park and H. J. Sung, *J. Mater. Chem. C*, 2013, **1**, 3138–3149.
17 M. Sookhakian, Y. Amin, S. Baradaran, M. Tajabadi, A. M. Golsheikh and W. Basirun, *Thin Solid Films*, 2014, **552**, 204–211.
18 Z.-S. Wu, G. Zhou, L.-C. Yin, W. Ren, F. Li and H.-M. Cheng, *Nano Energy*, 2012, **1**, 107–131.
19 S.-H. Yu, X. Cui, L. Li, K. Li, B. Yu, M. Antonietti and H. Cölfen, *Adv. Mater.*, 2004, **16**, 1636–1640.
20 W. T. Zheng, Y. M. Ho, H. W. Tian, M. Wen, J. L. Qi and Y. A. Li, *J. Phys. Chem. C*, 2009, **113**, 9164–9168.
21 C. Yang, N. Liu, W. Zeng, F. Long, Z. Song, J. Su, L. Li, Z. Zou, G. Fang and L. Xiong, *Nano Energy*, 2017, **33**, 280–287.
22 X. Yan, B.-K. Tay and P. Miele, *Carbon*, 2008, **46**, 753–758.
23 D. Shao, J. Gao, G. Xin, Y. Wang, L. Li, J. Shi, J. Lian, N. Koratkar and S. Sawyer, *Small*, 2015, **11**, 4785–4792.
24 D. Yuvaraj, R. Kaushik and K. Narasimha Rao, *ACS Appl. Mater. Interfaces*, 2010, **2**, 1019–1024.
25 D. Banerjee, S. H. Jo and Z. F. Ren, *Adv. Mater.*, 2004, **16**, 2028–2032.
26 C. Liang, L. Chen, D. Wu, C. Zhang, S. Xu, Y. Zhu, D. Xiong, P. Yang, L. Wang and P. K. Chu, *Mater. Lett.*, 2016, **172**, 40–43.
27 R. Tan, D. Wu, S. Xu, Y. Zhu, D. Xiong, L. Wang, P. Yang and P. K. Chu, *Electrochim. Acta*, 2016, **215**, 515–524.
28 D. Yuan, P. Ci, F. Tian, J. Shi, S. Xu, P. Xin, L. Wang and P. K. Chu, *J. Micro/Nanolithogr., MEMS, MOEMS*, 2009, **8**, 033012.
29 S. Xu, F. Wang, L. Mai, L. Wang and P. K. Chu, *Electrochim. Acta*, 2013, **90**, 344–349.
30 D. Wu, C. Zhang, C. Liang, Y. Zhu, S. Xu, D. Xiong, S. Xue, L. Wang and P. K. Chu, *J. Mater. Chem. C*, 2016, **4**, 2079–2087.
31 K. Jacobi, G. Zwicker and A. Gutmann, *Surf. Sci.*, 1984, **141**, 109–125.
32 T. Takahashi, H. Tokailin and T. Sagawa, *Phys. Rev. B: Condens. Matter Mater. Phys.*, 1985, **32**, 8317.
33 C. Arguello, D. Rousseau and S. P. d. S. Porto, *Phys. Rev.*, 1969, **181**, 1351.
34 G. J. Kovacs, I. Bertóti and G. Radnóczi, *Thin Solid Films*, 2008, **516**, 7942–7946.
35 S. Major, S. Kumar, M. Bhatnagar and K. Chopra, *Appl. Phys. Lett.*, 1986, **49**, 394–396.
36 M. N. Islam, T. Ghosh, K. Chopra and H. Acharya, *Thin Solid Films*, 1996, **280**, 20–25.
37 J. C. Fan and J. B. Goodenough, *J. Appl. Phys.*, 1977, **48**, 3524–3531.
38 C. D. Wagner, *Handbook of X-ray photoelectron spectroscopy: a reference book of standard data for use in X-ray photoelectron spectroscopy*, Physical Electronics Division, Perkin-Elmer Corp, 1979.
39 V. Frolov, A. Karabutov, S. Pimenov, V. Konov and V. Ageev, *Diamond Relat. Mater.*, 2001, **10**, 1719–1726.
40 J.-H. Lee, Y.-W. Chung, M.-H. Hon and I.-C. Leu, *Appl. Phys. A: Mater. Sci. Process.*, 2009, **97**, 403–408.
41 H. Yan, J. Wang and X. Zhong, *J. Mater. Sci.: Mater. Electron.*, 2011, **22**, 724–727.
42 Q. Zhao, H. Zhang, Y. Zhu, S. Feng, X. Sun, J. Xu and D. Yu, *Appl. Phys. Lett.*, 2005, **86**, 203115.
43 A. George, P. Kumari, N. Soin, S. Roy and J. McLaughlin, *Mater. Chem. Phys.*, 2010, **123**, 634–638.
44 S. Shi, J. Xu, X. Zhang and L. Li, *J. Appl. Phys.*, 2011, **109**, 103508.